Xu, M., Huang, H., Huang, Z., Wang, P., Wang, L., Xu, M., Mi, N., Yu, D., Yuan, X. (2018): Insight into the subducted Indian slab and origin of the Tengchong volcano in SE Tibet from receiver function analysis. - *Earth and Environmental Science Transactions of the Royal Society of Edinburgh*, *482*, pp. 567—579.

DOI: http://doi.org/10.1016/j.epsl.2017.11.048

Insight into the subducted Indian slab and origin of the Tengchong volcano in SE Tibet from receiver function analysis

Mijian Xu[1, 2], Hui Huang[1, 2, *], Zhouchuan Huang[1, 2, 3, 4, *], Pan Wang[1, 2], Liangshu Wang[1, 2], Mingjie Xu[1, 2], Ning Mi[1, 2], Hua Li[1, 2], Dayong Yu[1, 2] and Xiaohui Yuan[3]

1. State Key Laboratory for Mineral Deposits Research, School of Earth Sciences and Engineering, Nanjing University, Nanjing 210046, China
2. Institute of Geophysics and Geodynamics, Nanjing University, Nanjing 210046, China
3. GeoForschungsZentrum Potsdam, Telegrafenberg, 14473 Potsdam, Germany
4. Center of Modern Earth Sciences, Nanjing University, Nanjing 210046, China

*Corresponding authors: oldyellow9451@gmail.com (H. Huang);
huangz@nju.edu.cn (Z. Huang)

Abstract. The subduction of the Indian Plate beneath SE Tibet and its related volcanism in Tengchong are important geologic processes that accompany the evolution of the Tibetan Plateau. However, it is still not clear whether the subduction and volcanism are confined to the upper mantle or if they extend deep into the mantle transition zone (MTZ). Here, we imaged MTZ structures by using receiver function methods with the waveforms recorded by more than 300 temporary stations in SE Tibet. The results show significant depressions of both the 410-km and 660-km discontinuities and a thickened MTZ (260-280 km) beneath SE Tibet. The depression of the 660-km discontinuity (by 10-30 km) and the thickened MTZ correlate well with high P-wave velocity anomalies in the MTZ, indicating the presence of a subducted Indian slab within the MTZ. Significant depression of the 410-km discontinuity (by 10-20 km) beneath the Tengchong volcano indicates that the volcano originates from the MTZ and is closely related to the subducted Indian slab. Our results confirm the deep subduction of the Indian plate and the deep origin of the Tengchong volcano.

However, it remains unknown whether a slab gap exists and contributes to the Tengchong volcano.

Keywords: ChinArray; Tibet; Receiver function; Mantle discontinuity; Subduction

1. Introduction

The Tibetan Plateau (Fig. 1) formed from the collision of the Indian and Eurasian plates, which began ~50 Ma. The tectonic evolution and mechanism of growth of the Tibetan Plateau have long been the focus of geosciences (e.g., Tapponnier et al., 2001; Yin and Harrison, 2000). Deep mantle dynamics play an important role in the evolution of the Tibetan Plateau (e.g., Kind et al., 2002; Tapponnier et al., 2001). In SE Tibet, the Indian Plate is obliquely subducting eastward beneath Burma (Fig. 1) with active seismicity occurring down to ~200 km depth (Ni et al., 1989). However, the depth and extent of the slab is still under debate. Regional seismic tomography has provided clear images of the subducted slab as a high velocity body down to ~300-400 km depth but has produced blurred images at greater depths (Huang and Zhao, 2006; Huang et al., 2015b; Li et al., 2008). In contrast, teleseismic tomography has revealed notable high-velocity bodies in the MTZ (Huang et al., 2015a; Lei et al., 2009; Lei and Zhao, 2016). However, the resolution of the imaged Indian slab (especially in the MTZ) is relatively low because most seismic stations are located in the back-arc region (i.e., in Yunnan, SW China, ~400 km away from the arc) (Fig. 1). Our understanding of how deep the subducted slab extends and its interaction with the MTZ is inconclusive. Correspondingly, the origin of the active Tengchong volcano (last erupted in 1609) is still debated. Some models suggest that it is a subduction-driven volcano due to dehydration of the subducted Indian Plate and that it originates from the MTZ (Lei et al., 2009; Lei and

Zhao, 2016). Other models prefer a shallow origin, either induced by slab rollback (Lee et al., 2016; Ni et al., 2015; Richards et al., 2007) or mantle flow rising from a slab window in the subducted Indian slab (e.g., Guo et al., 2016; Zhang et al., 2017).

The MTZ structures, specifically the topographies of the 410 km and 660 km discontinuities (hereafter referred to as D410 and D660), provide important constraints on the depth extent of the slab because they are sensitive to the thermal anomalies near the MTZ. The D410 and D660, which describe sudden seismic velocity changes that are observed globally, reflect phase transitions of dominant minerals (i.e., olivine) in the mantle. The D410 is the result of the transition from olivine to wadsleyite, whereas the D660 represents the transition from ringwoodite to perovskite and magnesiowustite. Because of opposite Clapeyron slopes of the phase transitions at the D410 and D660, their depths vary oppositely due to thermal anomalies. In general, a cold slab causes a thicker MTZ due to an uplifted D410 and a depressed D660, while a hot plume leads to a thinner MTZ that results from a depressed D410 and an uplifted D660 (Bina and Helffrich, 1994). Global studies of MTZ structures have confirmed that the MTZ is thicker beneath subduction zones (e.g., West Pacific, South America) and is thinner beneath hot spots and plumes (e.g., South Pacific, Africa) (Lawrence and Shearer, 2006).

Receiver function analysis (Langston, 1979) is an important tool that enables the imaging of high-resolution MTZ structures. It has been widely used to study the D410 and D660 depths and the thermal anomalies within the MTZ under subduction zones, hotspots and plumes all over the world (e.g., Eagar et al., 2010; Li and Yuan, 2003; Tian et al., 2016). In this study, we calculated P-wave receiver functions (PRFs) with the waveforms recorded by a dense temporary network (ChinArray) to obtain high-resolution D410 and D660 topographies beneath SE Tibet. These results, together with 3-D P-wave velocity tomography, provide important clues for understanding the mantle dynamics and origin of the Tengchong volcano in SE Tibet.

2. Data and Methods

2.1 Waveform Data

In this study, we use the waveforms from 785 earthquakes with Mw > 5.5 and epicentral distances of 30°-90° (Fig. 1b) recorded at 398 three-component broadband stations (Fig. 1c). The stations belong to four seismic arrays. The first data set includes 325 temporary stations that were deployed between October 2011 and August 2012 by the ChinArray Project (inverted red triangles in Fig. 1c). The second data set consists of records from 24 permanent stations of the Chinese Seismic Network between January and June 2012 (yellow circles in Fig. 1c). The third data set includes 29 portable stations that were deployed by Nanjing University and the Chinese Academy of Sciences between January 2003 and August 2004 (green hexagons in Fig. 1c). The fourth data set includes data from 15 portable stations operated by the Massachusetts Institute of Technology between October 2003 and September 2004 (blue squares in Fig. 1c).

2.2 Receiver function deconvolution

We first removed the mean offset and linear trend of the waveforms, then filtered them with a Butterworth bandpass filter in the range of 0.05–2 Hz and rotated the horizontal components into radial and transverse components. We used the waveforms with a signal-to-noise ratio (SNR) greater than 7.0 dB on both the vertical and radial components. The SNR is calculated by:

$$SNR = 10log_{10}\left(\frac{A_S}{A_N}\right)^2 \quad (1)$$

where A_N and A_S are root mean squares (RMS) of the waveform in a 100-s time-window before and after theoretical P arrival times, respectively. We cut 130 s long vertical and radial waveforms (from 10 s before to 120 s after theoretical P arrival times) with high an SNR and then calculated the PRFs with an iterative time-domain deconvolution method (Ligorría and Ammon, 1999).

We applied strict criteria to select high quality PRFs. First, the cross-correlation coefficients between the original and recovered (convolution of PRF with vertical component) radial components are larger than 0.8 (i.e., more than 80% recovered). Second, the maximum amplitudes of PRFs in a 30-120 s window after the direct P (containing possible P410s and P660s phases) are smaller than 30% of the maximum amplitudes of the direct P phases. Finally, we manually checked all of the PRFs and removed those that had weak P phases, large negative amplitudes or harmonic oscillations. We obtained a total of 13,671 reliable PRFs. We sorted the PRFs by increasing epicentral distance and stacked them in every 1° bin to visually check the move-out of the converted phases. The converted phases (P410s, P660s) are clear around expected arrival times (Fig. 2), which suggests sharp velocity contrasts at the D410 and D660 and indicates that the quality of our data is good.

2.3 Receiver function migration

We migrated and stacked all PRFs with a common conversion points (CCP) method (Dueker and Sheehan, 1997; Eagar et al., 2010). We calculated the piercing points of PRFs at 300-800 km depths (the step is 1 km) with the standard 1-D AK135 model (Kennett et al., 1995) (Model I). Figure 3 shows good coverages of the Ps piercing points at 410 km and 660 km depths. We calculated the Ps-P differential times T_{Ps} in the spherical coordinate (Eagar et al., 2010):

$$T_{Ps} = \sum_i^N \left(\sqrt{\left(\frac{R_i}{\mathrm{Vs}_i}\right)^2 - {p_{Ps}}^2} - \sqrt{\left(\frac{R_i}{\mathrm{Vp}_i}\right)^2 - {p_P}^2} \right) \frac{\Delta r}{R_i}, \qquad (2)$$

where R_i is the Earth's radius for each i^{th} depth shell (r_i), Δr is the depth interval, p_P and p_{Ps} are ray parameters of direct P and Ps phases, respectively, and Vp_i and Vs_i are P and S wave velocities in the i^{th} layer, respectively. The amplitudes of the migrated receiver functions were linearly interpolated from PRFs according to the Ps-P differential times.

To investigate the effect of upper-mantle velocity heterogeneities in the RF migration, we employed a high-resolution, 3-D local P-wave velocity model (Huang et al., 2015a) (Model II) to remove potential effects of velocity heterogeneities in the upper mantle. The S-wave velocities are estimated based on the Vp/Vs ratio in the AK135 model due to the lack of a local S-wave velocity model in the study region. The Ps–P differential times in the 3-D model ($\mathrm{T_{Ps3D}}$) are derived as:

$$T_{Ps3D} = T_{Ps} + \Delta T, \qquad (3)$$

where ΔT is the time correction for the velocity perturbations in the 3-D velocity model.

2.4 CCP stacking

We set up grid nodes with 0.5° horizontal intervals (Figs. 3c and 3d) and searched for all of the migrated PRFs that are located in a circular bin (with 75 km radius) around each grid node at 1-km depth intervals. The numbers of PRFs at the D410 and D660 are larger than 300 at most grid nodes (Figs. 3c and 3d). We applied the bootstrapping method to resample the dataset and calculate the stacked amplitudes

2000 times. Then, the final mean PRFs and the corresponding 95% confidence level were calculated.

We searched for the P410s and P660s peaks in the migrated and stacked PRFs in the depth ranges of 370-450 km and 620-700 km, respectively. We only selected the peaks that had more than 60 individual PRFs at the corresponding grid nodes (Figs. 3c and 3d). They all have significantly positive amplitudes with lower boundaries above zero at a 95% confidence interval. We further calculated the MTZ thickness by subtracting the D410 depth from the D660 depth at each grid node.

3. Results

3.1 D410 and D660 topographies

Figure 4 shows the D410 and D660 depths obtained with 1-D and 3-D velocity models. We obtained ~400 peaks for both D410 and D660 from the stacked PRFs after a visual check. The D410 depression in the southwestern region is the dominant feature in both models. The D410 depths are generally deeper than 420 km, which are 10-20 km greater than in adjacent regions. In the northeastern region, however, the D410 depths (~410 km) are consistent with global averages. The D660 topography shows a similar pattern. In the western region (<104°E), the D660 depths are deeper, in the range of 670-690 km except where there is a local anomaly of <670 km under the Tengchong volcano. In the eastern region, the D660 depths are consistent with global averages of 660±10 km. In summary, the D410 and D660 are generally depressed in the western and southwestern regions of the study area where the Indian Plate subducts but are normal beneath the stable craton in the eastern regions.

3.2 Influence of 3-D velocity anomalies

To better estimate the influence of the 3-D velocity models (especially S-wave velocity or Vp/Vs ratio) on estimating the D410 and D660 depths, we constructed two more 3-D velocity models based on Model II. In the new models, S-wave velocity anomalies (dlnVs) are calculated from dlnVp based on numerical simulation (Cammarano et al., 2003) or global statistics (Saltzer et al., 2001). The variations in seismic velocities in the upper mantle are more sensitive to temperature variations than to compositional changes (Cammarano et al., 2003). However, P and S wave velocity perturbations have different sensitivities to temperature variations, resulting in different ratios of P and S wave anomalies (i.e., dlnVs/dlnVp ratio). In Model III, we calculated S wave velocities based on the dlnVs-dlnVp relationship by using forward calculations from the compositional elastic modules under the pressure and temperature conditions within the Earth (Cammarano et al., 2003). The corresponding dlnVs/dlnVp ratios are equal to approximately two in the upper mantle and in the MTZ. In addition, we constructed Model IV by estimating the S wave velocities based on global statistics between dlnVp and dlnVs in subduction zones (Saltzer et al., 2001). In this case, the mean dlnVs/dlnVp ratios are 2-3 in the 0-300 km depth range and are ~1.5 in the 300-1000 km depth range.

Figure 5 shows the D410 and D660 depths that were estimated with Models III and IV. The D410 and D660 topographies for the new models retain the major patterns that were generated in Model II, such as a significantly depressed D410 and D660 in the western and southwestern regions. However, both the D410 and D660 in the northeastern region, beneath the Yangtze Craton, are deeper than those in Model II by ~10 km. The Yangtze Craton is a stable craton with high-velocity anomalies in the upper mantle. The heat flow and temperature in the craton are much lower than those in adjacent regions (Hu et al., 2000). Thus, the dlnVs/dlnVp ratios should be smaller than those used in Models III and IV (Cammarano et al., 2003). Therefore, the D410 and D660 depths obtained with Models III and IV in the northeastern region are overestimated.

We performed further synthetic tests to estimate the uncertainties of the D410 and D660 depths beneath the Tengchong volcano. The input velocity model is modified from the AK135 1-D model. Initial -2.0% and +2.0% P-wave velocity anomalies (dlnVp) were added in the depth ranges of 50-410 km and 410-660 km (Fig. 6a), respectively. Similar S-wave velocity anomalies (dlnVs) were also added, but with larger amplitudes (dlnVs/dlnVp = 1.5, i.e., -3.0% and 3.0% in the upper mantle and MTZ, respectively). We first calculated theoretical time differences between the Ps (i.e., P410s and P660s) and P phases (T_{syn}=T_{Ps}-T_{P}) with the constructed velocity model (Fig. 6a; assuming vertical rays) and then inverted the synthetic data (T_{syn}) for the D410 and D660 depths with different velocity models that assume different dlnV (i.e., |dlnVp| from 0.0% to 4.0% with a step of 0.5%) and dlnVs/dlnVp ratios (from 0.5 to 2.0 with a step of 0.05). Both D410 and D660 depths inverted with a simple 1-D starting model (i.e., AK135 model, dlnV = 0.0%) (e.g., Model I) were significantly overestimated (Fig. 6). Specifically, the D410 is nearly 20 km deeper than the depth in the input model (Fig. 6b). Taking into account the 3-D velocity anomalies while assuming dlnVs/dlnVp = 1.0 (e.g., Model II) improves the result, the D410 are still significantly deeper than expected (Fig. 6b). The inverted D410 and D660 depths were closer to the input values when the dlnV or dlnVs/dlnVp ratios increase, and even became shallower than expected for very large dlnV and dlnVs/dlnVp ratios (e.g., Models III and IV in Figs. 6b and 6c).

We prefer the results of Model II to those of Models III and IV. The uncertainties of the estimated dlnVs/dlnVp ratios may introduce additional anomalies (Cammarano et al., 2003; Saltzer et al., 2001). In SE Tibet, the structural and thermal heterogeneities beneath the Tengchong volcano and the Yangtze Craton are strong. It is not appropriate to apply uniform dlnVs/dlnVp ratios for the whole region as done in Models III and IV. However, we must consider that the D410 and D660 depths beneath the Tengchong volcano may be overestimated by 10 km and 5 km, respectively, in Model II. In this case, the D410 depths are at least 420 km beneath the Tengchong volcano, still ~10 km deeper than adjacent regions.

3.3 MTZ thickness

Because the velocity anomalies in the upper mantle are common factors in estimating D410 and D660 depths, the MTZ thickness is independent of the velocity perturbations in the upper mantle and provides a better estimation of the thermal anomalies in the MTZ. The synthetic tests confirm that the deviation in the MTZ thickness is generally half of the deviations in the D410 and D660 depths (Fig. 6). Figures 4 and 5 also show the MTZ thicknesses beneath SE Tibet that were determined with different velocity models (Models I-IV). The results in these models (I-IV) are similar, which suggests that they are more reliable than the D410 and D660 topographies themselves. The MTZ thicknesses generally range from 230 km to 280 km and are thicker in the western region than in the eastern region. In the western region (i.e., <104°E), the MTZ thicknesses are generally greater than 260 km, except for a local anomaly beneath the Tengchong volcano where the MTZ thickness is less than 240 km. In the northeastern and southeastern regions, the MTZ thicknesses are ~250-260 km and ~240-250 km, respectively, which is in agreement with the global average of ~240-260 km (Lawrence and Shearer, 2006).

Zhang et al. (2017) also determined the MTZ structures in SE Tibet with a similar dataset. They constructed a 3-D model with P-wave velocities derived from the S-wave tomography using surface wave inversion (Li et al., 2013). The Vp/Vs ratio was derived from the AK135 model, i.e., dlnVs/dlnVp = 1.0 (which is similar to Model II in the present study). However, the S-wave tomography from long-period surface waves has relatively lower resolution and reveals only the S-wave structures down to ~300 km depth. Therefore, the velocity heterogeneities downward were not corrected in their model. Even so, their images are generally consistent with our results to the first order. Both the depressed D410 and D660, as well as thickened MTZ, are visible in the western region (<104°E), which confirms that the presence of these major features is robust.

4 Discussion

4.1 Thermal anomalies in the MTZ

The D410 and D660 topographies and the MTZ thicknesses are generally controlled by the phase transition of dominant minerals. Temperature is the most important factor that affects the phase transitions and the MTZ structures. The change in the MTZ thickness (δz) can be expressed as (Helffrich, 2000):

$$\delta z = \frac{\delta T * dz}{dP} * \left[\left(\frac{dP}{dT}\right)_{660} - \left(\frac{dP}{dT}\right)_{410}\right] \qquad (4)$$

where $\frac{dP}{dz}$ ($35\,MPa/km$) is the pressure gradient in the Earth, $\left(\frac{dP}{dT}\right)_{410}$ ($3.1\,MPa/K$) and $\left(\frac{dP}{dT}\right)_{660}$ ($-2.6\,MPa/K$) are Clapeyron slops of D410 and D660, respectively (Akaogi et al., 2007). Lateral variations of 30 km in the MTZ thickness indicate a temperature variation of ~200 K, which causes P-wave velocity anomalies by ~1% (Cammarano et al., 2003; Deal et al., 1999). Thus, in the western region, the thickened MTZ (up to 280 km) suggests ~200 K lower temperature in the MTZ and therefore an

~1% higher P-wave velocity. The predicted velocity anomalies are comparable to those revealed by seismic tomography (Fig. 7).

Figure 8 compares the stacked PRFs (determined with model II) with the P-wave velocity anomalies (Huang et al., 2015a) along three profiles in SE Tibet. There are overall good correlations between the seismic images and the D410 and D660 topographies. The deeper and shallower D410 is found in low and high velocity zones, respectively, whereas D660 has opposite relationships (i.e., deeper in high velocity zones and shallower in low velocity zones). Because velocity anomalies result from thermal anomalies in general, our images closely follow the Clapeyron slopes of phase transitions for the dominant minerals at these discontinuities.

In the eastern region (>104°E), the D410 and D660 are flat without visible deviations from the global averages, although P-wave images also show significant velocity anomalies. A possible explanation is less thermal activity in the MTZ under the eastern region (in general, under the Yangtze Craton) than under the western region (in the subduction domain), as discussed later.

4.2 Subduction of the Indian Plate

The tectonic evolution of the Indo-Burma range is dominated by the oblique subduction of the Indian Plate beneath SE Tibet (Ni et al., 2015, 1989), which is a transition zone from oceanic subduction along the Sunda Arc in SE Asia to continental collision between the Indian and Eurasian plates (Huang et al., 2015b; Li et al., 2008; Pesicek et al., 2010; Wei et al., 2012). Seismic images argue whether the subducted slab in SE Tibet reaches the MTZ or whether it is confined to the upper mantle. Our CCP stacking images show that D660 is depressed and the MTZ is thickened significantly in SE Tibet, which is similar to observations in other subduction zones such as the NW Pacific (Li and Yuan, 2003; Tian et al., 2016). The most plausible explanation for the depressed D660 is a lower temperature within the subducted slab, which is imaged as high velocity bodies in the MTZ. The thickened MTZ in the study region is mostly caused by the D660 depression. In this case, the ~30 km depressed D660 indicates that the temperature near D660 is 400 K lower than in adjacent regions. It would cause ~+2% perturbations in P-wave velocity, which correlates well with seismic tomography (Fig. 8).

Water content may also significantly affect the D410 and D660 depths (Helffrich, 2000; Higo et al., 2001; Litasov et al., 2005). Studies on ultra-deep diamonds have indicated that stagnant slabs lying in the MTZ could release water into the surrounding mantle (e.g., Harte, 2010; Pearson et al., 2014). The ringwoodite-to-perovskite transition occurs at greater depths if hydrous ringwoodite exists (Higo et al., 2001). A water content of 2.0 wt% in the subducted slab may induce a D660 depression by ~15 km (Cao and Levander, 2010). Therefore, the significant depression of D660 in the western region (<104°E) is also possibly affected by water that was released from the subducted Indian slab.

Zhang et al. (2017) attributed the depressed D660 and high velocity anomalies to the presence of detached lithosphere in SE Tibet. Figure 9 shows a 3-D distribution of the high ($dlnVp \geq 1.0\%$) and low velocity ($dlnVp \leq -1.0\%$) bodies in the upper mantle and MTZ beneath SE Tibet. It shows some indications of the detached lithosphere, but the corresponding high velocity body is very limited and is only constrained to be shallower than 500 km. Therefore, we prefer that the high velocity bodies at the bottom of the MTZ represent the subducted Indian slab, rather than the detached lithosphere.

In any case, we confirm the deeply subducted slab in the MTZ or even in the lower mantle. However, it is not clear whether the subducted slab in the MTZ is connected with the subducted Indian slab in the upper mantle. It may also represent a remnant Tethyan slab during the closure of the paleo Tethyan ocean (e.g., van der Voo, 1999). The receiver function study in the Indochina Peninsula show that the D660 depression continues southward in a N-S belt until ~12°N (Yu et al., 2017) where seismic tomography clearly revealed a continuous subducted slab from surface to the MTZ (Huang et al., 2015b; Pesicek et al., 2010). Therefore, it is more appropriate to relate the slab beneath SE Tibet to the present subduction of the Indian Plate. SE Tibet is located in a transition region from oceanic subduction in SE Asia to continental subduction (or collision) in south Tibet. The subducted slab seems broken beneath SE Tibet (e.g., Huang et al., 2015b; Pesicek et al., 2010; Wei et al., 2012), so that the oceanic part of the Indian Plate probably continues to sink deeply in the MTZ while the Indo-Burma ranges are formed by the accretionary tectonics associated with continental subduction. The age of the oceanic lithosphere in the northeastern Indian Ocean is ~100 Myr and is comparable to that in Java (Müller et al., 2008) (Fig. 1a). It is not surprising that the subducted oceanic Indian slab sinks into the MTZ when it is driven by the ongoing northeastward motion of the Indian Plate; however, it is difficult for the continental part of the Indian Plate to subduct into the deep mantle because it generally has a lower density. Thus, the slab may be torn, forming a gap between the subducted continental slab in the upper mantle and the subducted oceanic slab in the MTZ. However, the present-day dataset for this region is insufficient to locate the potential slab gap.

4.3 Origin of the Tengchong volcano

The origin of the Tengchong volcano is still under debate. One model argues that the dehydration of the deeply subducted Indian slab induces mantle upwelling from the MTZ (Lei et al., 2009; Lei and Zhao, 2016; Zhao et al., 2007, 2009). In contrast, other models prefer that the rollback of the Indian slab or slab-tearing which creates a slab window, allowing sub-slab hotter mantle to rise to the Tengchong volcano (e.g., Ni et al., 2015; Zhang et al., 2017). The significant D410 depression is predictable according to the first hypothesis due to heat anomalies or fluids beneath the active volcano but is not predictable in the latter models. In this study, we found a significant localized D410 depression by 10-20 km (Figs. 4 and 5) beneath the Tengchong volcano. Our comprehensive synthetic tests exclude the influence of the 3-D velocity heterogeneities and confirm that the D410 depression is reliable (Fig. 6), suggesting that the Tengchong volcano originates from the MTZ or at least from the D410.

Although seismic tomography is not capable of producing reliable seismic images in the upper mantle beneath Myanmar due to the poor station coverage, the present dataset could provide some constraints on the origin of the volcano. Because most stations are located to the east of the volcano, the ray paths from teleseismic events generally incline eastward and induce strong smearing effects. Figure 10 shows synthetic tests with teleseismic ray paths that were recorded by the seismic stations (see Huang et al., 2015a for details). If the Tengchong volcano is caused by sub-slab flow from a slab gap at ~200 km (e.g., Zhang et al., 2017), there should be an eastward-inclined low velocity body that connects the volcano and the slab gap (Fig. 10c). However, the actual inversion reveals a westward-inclined low velocity body; a high velocity body at 200-400 km depths to the west of the volcano is necessary to produce such seismic images (Fig. 10d). Therefore, the Tengchong volcano is not related directly to a slab gap at ~200 km. Instead, an apparent eastward-inclined low velocity body is found beneath the eastern Himalayan Syntax (~300 km northward)

(Fig. 9b), which may be indicative of a slab gap. However, it is difficult to associate it with the Tengchong volcano.

The depressed D410 and westward-inclined low velocity bodies extending down to ~400 km beneath the Tengchong volcano (Figs. 8 and 9) confirm that the volcano is sourced deeply from the MTZ, rather than a shallow origin at ~200 km. Because of the depressed D410 but normal D660, the MTZ thicknesses beneath the Tengchong volcano are ~230-240 km, which are 10-20 km thinner than the global average. The D410 depression indicates a hot thermal anomaly according to the positive Clapeyron slope of the olivine-to-wadsleyite transition (Bina and Helffrich, 1994). The D410 depression by 20 km suggests a hot thermal anomaly of ~200 K near the D410 under the Tengchong volcano according to equation (4). Another influence may be elevated water content in the MTZ beneath the Tengchong volcano, which was released from the subducted Indian slab. The dehydration reactions in the MTZ cause significant fluid transportation and generate a hot melt layer above D410 (Hebert and Montési, 2013; Zhao et al., 2007). We also observed negative converted phases above D410 in our images (Fig. 8). The negative Ps phases are more visible and show double phases under the Tengchong volcano compared with surrounding regions. Therefore, the double Ps phases indicate the release of more water and transportation under the Tengchong volcano, which may be related to the subducted Indian slab (e.g., Lei and Zhao, 2016; Zhao et al., 2007, 2009). Numerical simulations also prove that mantle upwelling could be induced at 400-500 km by the subducted slab into the MTZ; the subducted crust plays an essential role in triggering this upwelling (Li et al., 2011).

Some geochronological and geochemical studies have observed mafic and intermediate dykes along the western margin of the Indochina Block (e.g., *Arboit* et al., 2016). They proposed mantle upwelling to explain partial melting from the enriched asthenospheric mantle (e.g., *Arboit* et al., 2016; Guo et al., 2015). As mentioned earlier, SE Tibet is located at the transition point from oceanic subduction in SE Asia to continental subduction in south Tibet. There is probably a slab window between the subducted Indian slab in the upper mantle and the stagnant slab in the MTZ. The sinking slab segment is capable of producing decompression melting in the upper mantle and induced the mantle upwelling in a return flow system (*Faccenna* et al., 2010). We have shown that the subducted Indian slab is continuous in the upper mantle (down to 400 km). The slab window, if it exists, is probably located in the MTZ. Accordingly, mantle upwelling through the slab window could lead to a depressed D410 and thinner MTZ (Yu et al., 2017). Although seismic tomography revealed an apparent slab window in the MTZ beneath the Tengchong volcano (Fig. 9), it is more likely caused by the vertical smearing from tomographic inversion. More stations in Myanmar are necessary to better reveal the slab structures.

An important and interesting result is that the D410 and D660 depressions are not located immediately beneath the Tengchong volcano but are ~100 km and ~200 km eastward, respectively (Fig. 8). It is consistent with the westward-inclined low-velocity body in the upper mantle. The images indicate that mantle upwelling is dynamically influenced by approximately westward-directed horizontal flow in the upper mantle. One straightforward mechanism is the rollback of the subducted Indian slab and induced horizontal return flow toward the trench in the upper mantle (e.g., Ni et al., 2015). It may also account for the partial melting composition from the enriched asthenospheric mantle observed in geochemical studies (e.g., Lee et a., 2016).

5 Conclusions

We used the receiver function CCP stacking method to reveal MTZ structures beneath SE Tibet. We determined the MTZ structures with both 1-D and 3-D velocity models. The 3-D models are important to remove the influence of velocity anomalies in the upper mantle. The most important results are the depressed D410 and D660 as well as thickened MTZ in the western region where the Indian Plate subducts into the MTZ.

The D410 is generally deeper (>420 km) in the southwest than that in the northeast (~410 km). The D410 depressions correlate well with the low velocity zones in the upper mantle (from the surface to a 400-km depth) beneath the volcano. The D660 is deeper than 680 km in a broad region beneath the Tengchong volcano, where the MTZ is thickened by ~20 km (i.e., 260-290 km). The depressed D660 and thickened MTZ are consistent with the high velocity anomalies in the MTZ and indicate the presence of a cold slab at the bottom of the MTZ. The images confirm that the subducted Indian slab in the MTZ affects the structures near D660. The depressed D410 suggests that the Tengchong volcano originates from the MTZ and is closely related to the subducted Indian slab.

However, it is not clear whether the subducting Indian slab in the upper mantle is connected with the stagnant slab in the MTZ. A slab window may exist and may contribute to the Tengchong volcano. Unfortunately, the present-day stations cannot image the slab structures clearly. More stations need to be deployed in Myanmar to improve our understanding of the upper mantle structures and dynamics in SE Tibet.

Acknowledgements. This work was supported by the ChinArray Program (DQJB16A0306), the National Natural Science Foundations of China (41674044, 41404038), and the Natural Science Foundation of Jiangsu Province (Grant: BK20130570). ZH is also supported by the Deng Feng Scholar Program of Nanjing

University and the Alexander von Humboldt Foundation. The waveform data were provided by the China Seismic Array Data Management Center at the Institute of Geophysics, China Earthquake Administration and Data Management Center of Incorporated Research Institutions for Seismology (IRIS). We thank Prof. An Yin (editor), Dapeng Zhao, Frederik Tilmann and an anonymous reviewer for their constructive comments. Most figures were made using GMT (Wessel et al., 2013); Figure 9 was made with Paraview (www.paraview.org).

References:

Akaogi, M., Takayama, H., Kojitani, H., Kawaji, H., Atake, T., 2007. Low-temperature heat capacities, entropies and enthalpies of Mg2SiO4 polymorphs, and α−β−γ and post-spinel phase relations at high pressure. Phys. Chem. Miner. 34, 169–183.

Arboit, F., Collins, A.S., Morley, C.K., Jourdan, F., King, R., Foden, J. Amrouch, K., 2016. Geochronological and geochemical studies of mafic and intermediate dykes from the Khao Khwang Fold-Thrust Belt: Implications for petrogenesis and tectonic evolution, Gondwana Res. 36, 124–141.

Argus, D.F., Gordon, R.G., DeMets, C., 2011. Geologically current motion of 56 plates relative to the no-net-rotation reference frame. Geochem. Geophys. Geosystems 12, Q11001.

Bina, C.R., Helffrich, G., 1994. Phase transition Clapeyron slopes and transition zone seismic discontinuity topography. J. Geophys. Res. Solid Earth 99, 15853–15860.

Bird, P., 2003. An updated digital model of plate boundaries. Geochem. Geophys. Geosystems 4, 1027.

Cammarano, F., Goes, S., Vacher, P., Giardini, D., 2003. Inferring upper-mantle temperatures from seismic velocities. Phys. Earth Planet. Inter. 138, 197–222.

Cao, A., Levander, A., 2010. High-resolution transition zone structures of the Gorda Slab beneath the western United States: Implication for deep water subduction. J. Geophys. Res. Solid Earth 115, B07301.

Chen, C., Zhao, D., Tian, Y., Wu, S., Hasegawa, A., Lei, J., Park, J.-H., Kang, I.-B., 2017. Mantle transition zone, stagnant slab and intraplate volcanism in Northeast Asia. Geophys. J. Int. doi:10.1093/gji/ggw491

Deal, M.M., Nolet, G., van der Hilst, R.D., 1999. Slab temperature and thickness from seismic tomography: 1. Method and application to Tonga. J. Geophys. Res. Solid Earth 104, 28789–28802.

Dueker, K.G., Sheehan, A.F., 1997. Mantle discontinuity structure from midpoint stacks of converted P to S waves across the Yellowstone hotspot track. J. Geophys. Res. Solid Earth 102, 8313–8327.

Eagar, K.C., Fouch, M.J., James, D.E., 2010. Receiver function imaging of upper mantle complexity beneath the Pacific Northwest, United States. Earth Planet. Sci. Lett. 297, 141–153.

Faccenna, C., Becker, T.W., Lallenmand, S., Lagabrielle, Y., Funiciello, F., Piromallo, C., 2010. Subduction-triggered magmatic pulses: A new class of plumes?, Earth Planet. Sci. Lett. 299, 54–68.

Gripp, A.E., Gordon, R.G., 2002. Young tracks of hotspots and current plate velocities. Geophys. J. Int. 150, 321–361.

Guo, X., Gao, R., Li, S., Xu, X., Huang, X., Wang, H., Li, W., Zhao, S., Li, X., 2016. Lithospheric architecture and deformation of NE Tibet: New insights on the interplay of regional tectonic processes. Earth Planet. Sci. Lett. 449, 89–95.

Guo, Z., Cheng, Z., Zhang, M., Zhang, L., Li, X., Liu, J., 2015. Post-collisional high-

K calc-alkaline volcanism in Tengchong volcanic field, SE Tibet: constraints on Indian eastward subduction and slab detachment. J. Geol. Soc. 172, 624–640.

Harte, B., 2010. Diamond formation in the deep mantle: the record of mineral inclusions and their distribution in relation to mantle dehydration zones. Mineral. Mag. 74, 189–215.

Hebert, L.B., Montési, L.G.J., 2013. Hydration adjacent to a deeply subducting slab: The roles of nominally anhydrous minerals and migrating fluids. J. Geophys. Res. Solid Earth 118, 2013JB010497.

Helffrich, G., 2000. Topography of the transition zone seismic discontinuities. Rev. Geophys. 38, 141–158.

Higo, Y., Inoue, T., Irifune, T., Yurimoto, H., 2001. Effect of water on the spinel-postspinel transformation in Mg2SiO4. Geophys. Res. Lett. 28, 3505–3508.

Hu, S., He, L., Wang, J., 2000. Heat flow in the continental area of China: a new data set. Earth Planet. Sci. Lett. 179, 407–419.

Huang, J., Zhao, D., 2006. High-resolution mantle tomography of China and surrounding regions. J. Geophys. Res. Solid Earth 111, B09305.

Huang, Z., Wang, P., Xu, M., Wang, L., Ding, Z., Wu, Y., Xu, M., Mi, N., Yu, D., Li, H., 2015a. Mantle structure and dynamics beneath SE Tibet revealed by new seismic images. Earth Planet. Sci. Lett. 411, 100–111.

Huang, Z., Zhao, D., Wang, L., 2015b. P wave tomography and anisotropy beneath Southeast Asia: Insight into mantle dynamics. J. Geophys. Res. Solid Earth 120, 2015JB012098.

Kennett, B.L.N., Engdahl, E.R., Buland, R., 1995. Constraints on seismic velocities in the Earth from traveltimes. Geophys. J. Int. 122, 108–124.

Kind, R., Yuan, X., Saul, J., Nelson, D., Sobolev, S.V., Mechie, J., Zhao, W., Kosarev, G., Ni, J., Achauer, U., Jiang, M., 2002. Seismic Images of Crust and Upper Mantle Beneath Tibet: Evidence for Eurasian Plate Subduction. Science 298, 1219–1221.

Langston, C.A., 1979. Structure under Mount Rainier, Washington, inferred from teleseismic body waves. J. Geophys. Res. Solid Earth 84, 4749–4762.

Lawrence, J.F., Shearer, P.M., 2006. A global study of transition zone thickness using receiver functions. J. Geophys. Res. Solid Earth 111, B06307.

Lee, H.-Y., Chung, S.-L., Yang, H.-M., 2016. Late Cenozoic volcanism in central Myanmar: Geochemical characteristics and geodynamic significance. Lithos, Recent advances on the tectonic and magmatic evolution of the Greater Tibetan Plateau: A Special Issue in Honor of Prof. Guitang Pan 245, 174–190.

Lei, J., Zhao, D., 2016. Teleseismic P-wave tomography and mantle dynamics beneath Eastern Tibet. Geochem. Geophys. Geosystems 17, 1861–1884.

Lei, J., Zhao, D., Su, Y., 2009. Insight into the origin of the Tengchong intraplate volcano and seismotectonics in southwest China from local and teleseismic data. J. Geophys. Res. Solid Earth 114, B05302.

Li, C., van der Hilst, R.D., Meltzer, A.S., Engdahl, E.R., 2008. Subduction of the Indian lithosphere beneath the Tibetan Plateau and Burma. Earth Planet. Sci. Lett. 274, 157–168.

Li, X., Yuan, X., 2003. Receiver functions in northeast China – implications for slab penetration into the lower mantle in northwest Pacific subduction zone. Earth Planet. Sci. Lett. 216, 679–691.

Li, Y., Wu, Q., Pan, J., Zhang, F., Yu, D., 2013. An upper-mantle S-wave velocity model for East Asia from Rayleigh wave tomography. Earth Planet. Sci. Lett. 377–378, 367–377.

Li, Z.H., Xu, Z.Q., Gerya, T.V., 2011. Flat versus steep subduction: Contrasting modes for the formation and exhumation of high- to ultrahigh-pressure rocks in continental collision zones. Earth Planet. Sci. Lett. 301, 65–77.

Ligorría, J.P., Ammon, C.J., 1999. Iterative deconvolution and receiver-function estimation. Bull. Seismol. Soc. Am. 89, 1395–1400.

Litasov, K.D., Ohtani, E., Sano, A., Suzuki, A., Funakoshi, K., 2005. Wet subduction versus cold subduction. Geophys. Res. Lett. 32, L13312.

Müller, R.D., Sdrolias, M., Gaina, C., Roest, W.R., 2008. Age, spreading rates, and spreading asymmetry of the world's ocean crust. Geochem. Geophys. Geosystems 9, Q04006.

Ni, J., Holt, W.E., Flesch, L.M., Sandvol, E.A., Hearn, T.M., Schmerr, N.C., 2015. Late Cenozoic deformation of the Eurasian and Burma Plates due to subduction of the Indian Plate beneath SE Tibetan Plateau and Myanmar. AGU Fall Meet. Abstr. 34.

Ni, J.F., Guzman-Speziale, M., Bevis, M., Holt, W.E., Wallace, T.C., Seager, W.R., 1989. Accretionary tectonics of Burma and the three-dimensional geometry of the Burma subduction zone. Geology 17, 68–71.

Pearson, D.G., Brenker, F.E., Nestola, F., McNeill, J., Nasdala, L., Hutchison, M.T., Matveev, S., Mather, K., Silversmit, G., Schmitz, S., Vekemans, B., Vincze, L., 2014. Hydrous mantle transition zone indicated by ringwoodite included within diamond. Nature 507, 221–224.

Pesicek, J.D., Thurber, C.H., Widiyantoro, S., Zhang, H., DeShon, H.R., Engdahl, E.R., 2010. Sharpening the tomographic image of the subducting slab below Sumatra, the Andaman Islands and Burma. Geophys. J. Int. 182, 433–453.

Richards, S., Lister, G., Kennett, B., 2007. A slab in depth: Three-dimensional geometry and evolution of the Indo-Australian plate. Geochem. Geophys. Geosystems 8, Q12003.

Saltzer, R.L., van der Hilst, R.D., Kárason, H., 2001. Comparing P and S wave heterogeneity in the mantle. Geophys. Res. Lett. 28, 1335–1338.

Tapponnier, P., Zhiqin, X., Roger, F., Meyer, B., Arnaud, N., Wittlinger, G., Jingsui, Y., 2001. Oblique Stepwise Rise and Growth of the Tibet Plateau. Science 294, 1671–1677.

Tian, Y., Zhu, H., Zhao, D., Liu, C., Feng, X., Liu, T., Ma, J., 2016. Mantle transition zone structure beneath the Changbai volcano: Insight into deep slab dehydration and hot upwelling near the 410 km discontinuity. J. Geophys. Res. Solid Earth 121, 2016JB012959.

Van der Voo, R., W. Spakman, and H. Bijwaard (1999), Tethyan subducted slabs under India, Earth Planet. Sci. Lett., 171(1), 7–20.

Wei, W., Xu, J., Zhao, D., Shi, Y., 2012. East Asia mantle tomography: New insight into plate subduction and intraplate volcanism. J. Asian Earth Sci. 60, 88–103.

Wessel, P., Smith, W.H.F., Scharroo, R., Luis, J., Wobbe, F., 2013. Generic Mapping Tools: Improved Version Released. Eos Trans. Am. Geophys. Union 94, 409–410.

Yin, A., Harrison, T.M., 2000. Geologic Evolution of the Himalayan-Tibetan Orogen. Annu. Rev. Earth Planet. Sci. 28, 211–280.

Yu, Y., Gao, S.S., Liu, K.H., Yang, T., Xue, M., Le, K.P., 2017. Mantle transition zone discontinuities beneath the Indochina Peninsula: Implications for slab subduction and mantle upwelling. Geophys. Res. Lett. 44, 7159-7167.

Zhang, R., Wu, Y., Gao, Z., Fu, Y.V., Sun, L., Wu, Q., Ding, Z., 2017. Upper mantle discontinuity structure beneath eastern and southeastern Tibet: New constraints on the Tengchong intraplate volcano and signatures of detached lithosphere under the western Yangtze Craton. J. Geophys. Res. Solid Earth 2016JB013551.

Zhao, D., Maruyama, S., Omori, S., 2007. Mantle dynamics of Western Pacific and East Asia: Insight from seismic tomography and mineral physics. Gondwana Res. 11, 120–131.

Zhao, D., Tian, Y., Lei, J., Liu, L., Zheng, S., 2009. Seismic image and origin of the Changbai intraplate volcano in East Asia: Role of big mantle wedge above the stagnant Pacific slab. Phys. Earth Planet. Inter. 173, 197–206.

Figure captions:

Fig. 1: (a) Tectonics in the Tibetan Plateau and SE Asia. The purple lines denote the plate boundaries (Bird, 2003). The age of the oceanic lithosphere (Müller et al., 2008) is shown in different colors. The black and yellow arrows denote the absolute plate-motion directions of the surrounding plates in HS3-Nuvel-1A (Gripp and Gordon, 2002) and NNR-MORVEL56 models (Argus et al., 2011), respectively. The red triangles denote active volcanoes. TC represents the Tengchong volcano. (b) Teleseismic events used in the study (red dots). The three great circles denote the epicentral distances of 30°, 60°, and 90°, respectively. (c) Distribution of the 398 stations used in the study. Inverted red triangles denote the 325 portable stations deployed by the ChinArray project. Blue squares denote the 15 portable stations deployed by the Massachusetts Institute of Technology (MIT). Yellow circles denote the 21 permanent stations operated by the Chinese Seismic Network (CSN). Green circles denote the 29 portable stations deployed by Nanjing University and the Chinese Academy of Sciences (NJU-CAS). Solid magenta lines denote major tectonic boundaries in SE Tibet. The dashed magenta lines show the depth of the subducted Indian slab (Ni et al., 1989). The red triangle denotes the Tengchong volcano.

Fig. 2: (a) Stacked P-wave receiver functions in each 1°-bin plotted against the epicentral distances. Red and blue colors denote the positive and negative pulses, respectively. Dashed lines denote the theoretical arrival times for different phases predicted with the reference 1-D AK135 model. (b) Numbers of P-wave receiver functions in different epicentral distances.

Fig. 3: (a, b) Ps piercing points at 410-km (blue dots) and 660-km (red dotes) depths. Yellow triangles denote the stations. (c, d) Number of points within each circular

bin (with radius of 75 km) at 410 km and 660 km depths.

Fig. 4: (a-c) Depths of the 410- and 660-km discontinuities and MTZ thicknesses, determined with the 1-D AK135 model (I). (d-f) The same as (a-c) but for the results determined with the 3-D velocity model (II) (see the text for details).

Fig. 5: The same as Fig. 4 but for the two other 3-D models (III and IV; see the text for details).

Fig. 6: Synthetic tests for receiver function migration, estimating the influence of different velocity models on the calculated D410 and D660 depths. (a) The synthetic 1-D velocity model beneath the Tengchong volcano used for calculating the synthetic (T_{Ps}-T_P) data sets. (b) The inverted D410 depths (blue lines) using different velocity anomalies (dlnV=|dlnVp|) and dlnVs/dlnVp ratios. Red dashed lines show the input model for calculating the synthetic data. Symbols I-IV denote the approximate locations of the actual inversions with different velocity models in the study (See the text for details). (c) and (d) are the same as (b) but for the D660 depths and MTZ thickness, respectively.

Fig. 7: Comparison of the MTZ thicknesses (contour lines) and the mean P-wave velocity anomalies (background colors) in the MTZ. Blue and red colors denote high and low velocities, respectively. Blue and red contours denote thick and thin MTZ, respectively.

Fig. 8: Comparison of the stacked P-wave receiver functions and the P-wave velocity anomalies (Huang et al., 2015a) along the three profiles shown in the bottom-right figure. Blue and red colors in background denote high and low velocities, respectively. Black and gray lines denote the average P-wave receiver functions and their 95% confidence level, respectively, obtained from 2,000 bootstrapping iterations (see the text for details). Red and blue colors denote the

significant positive and negative pulses, respectively. Two dashed horizontal lines denote the 410 km and 660 km depths for reference. The red triangle denotes the Tengchong volcano.

Fig. 9: (a) 3-D illustration of the high velocity bodies ($dlnVp \geq 1.0\%$) in the upper mantle beneath SE Tibet. Colors denote the depths using the scale shown at the bottom. Yellow lines denote the province boundaries in China. Red squares show the Tengchong volcano (TC) and its projection at a 410-km depth for reference. (b) 3-D illustration of the low velocity bodies ($dlnVp \leq -1.0\%$) in the upper mantle beneath SE Tibet.

Fig. 10: Synthetic tests for smearing effects of the low velocity body beneath the Tengchong volcano. (a) Locations of the stations (inverted triangles) and the velocity anomalies (A and B). (b, c, d) Cross sections of three different synthetic tests. Left and right figures show the input models and output results, respectively. The horizontal dashed lines denote the Moho, D410 and D660.

Figure
Click here to download Figure: figures2.pdf

Figure 1

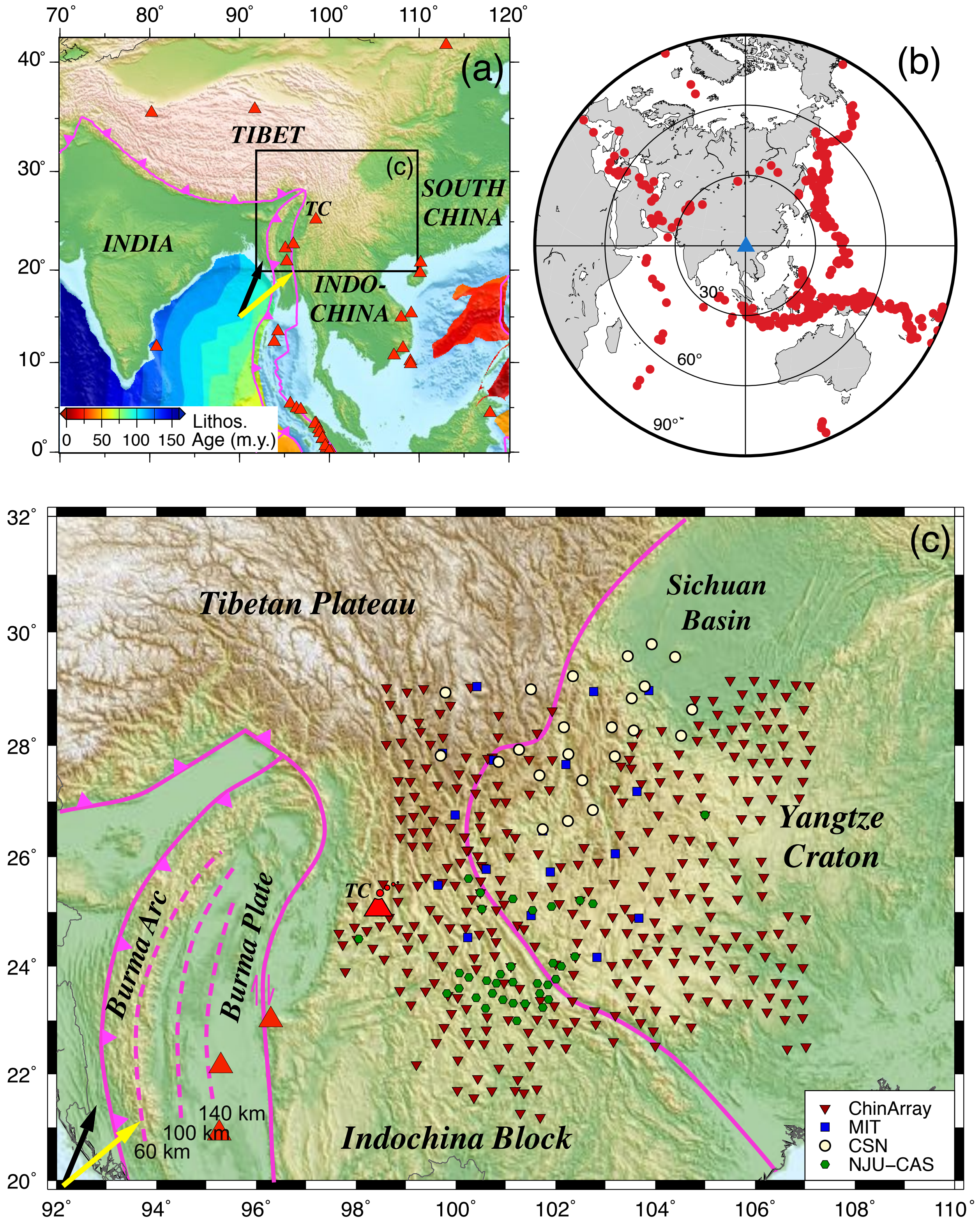

Figure 2

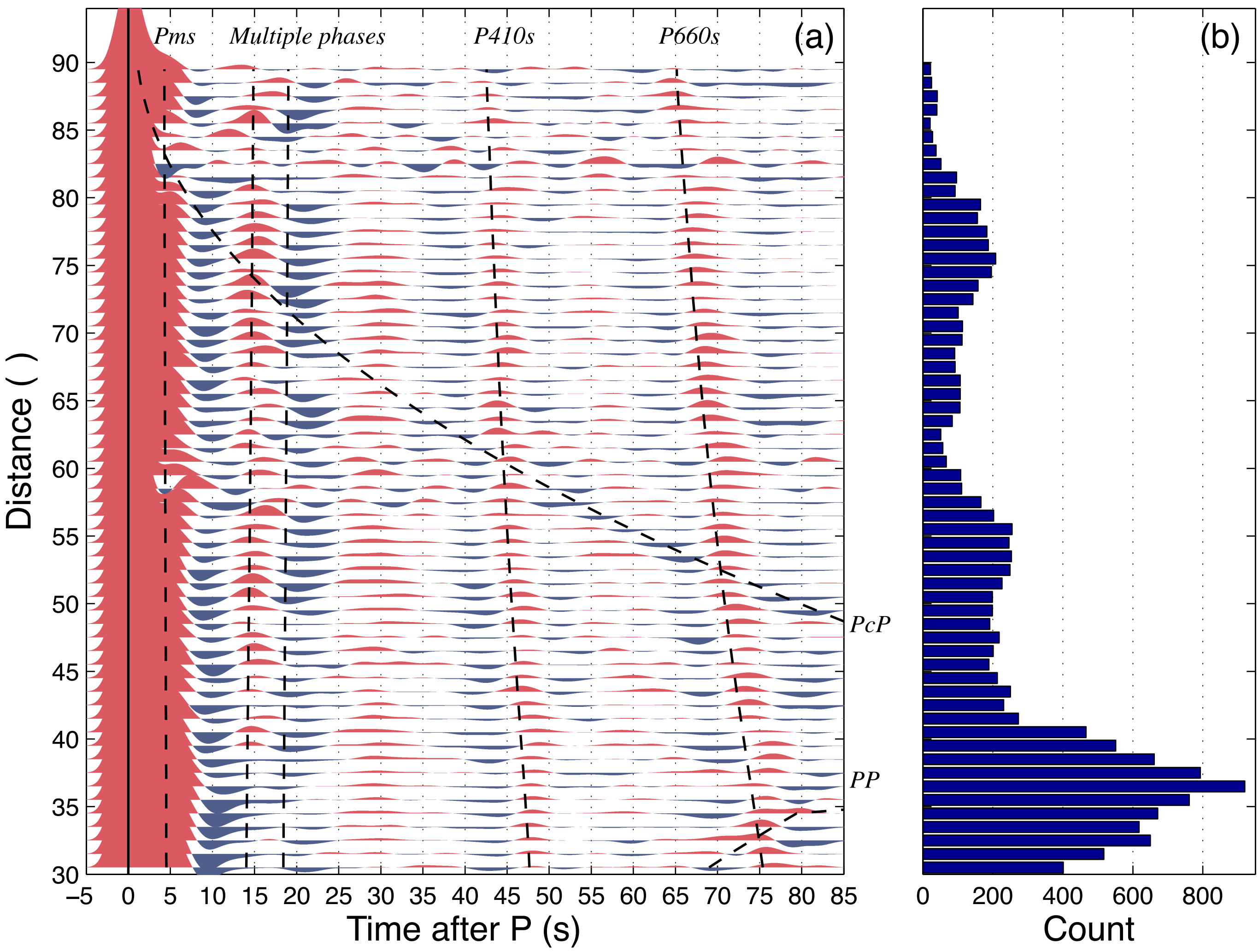

Pms
Multiple phases
P410s
P660s
(a)
(b)
PcP
PP
Distance ( )
Time after P (s)
Count

Figure 4

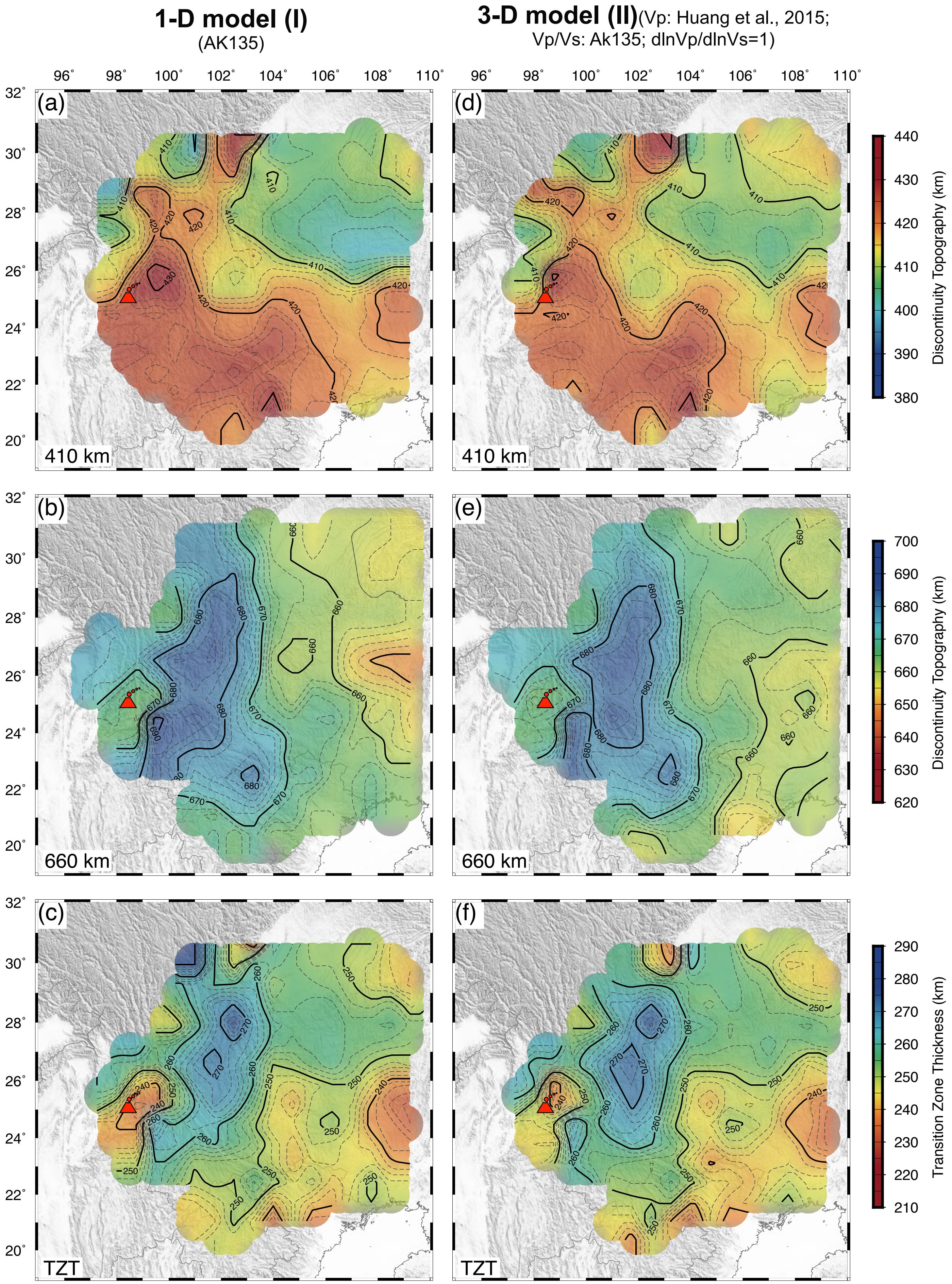

1-D model (I)
(AK135)
3-D model (II)(Vp: Huang et al., 2015;
Vp/Vs: Ak135; dlnVp/dlnVs=1)
(a)
(b)
(c)
(d)
(e)
(f)
410 km
660 km
TZT
Discontinuity Topography (km)
Transition Zone Thickness (km)

Figure 5

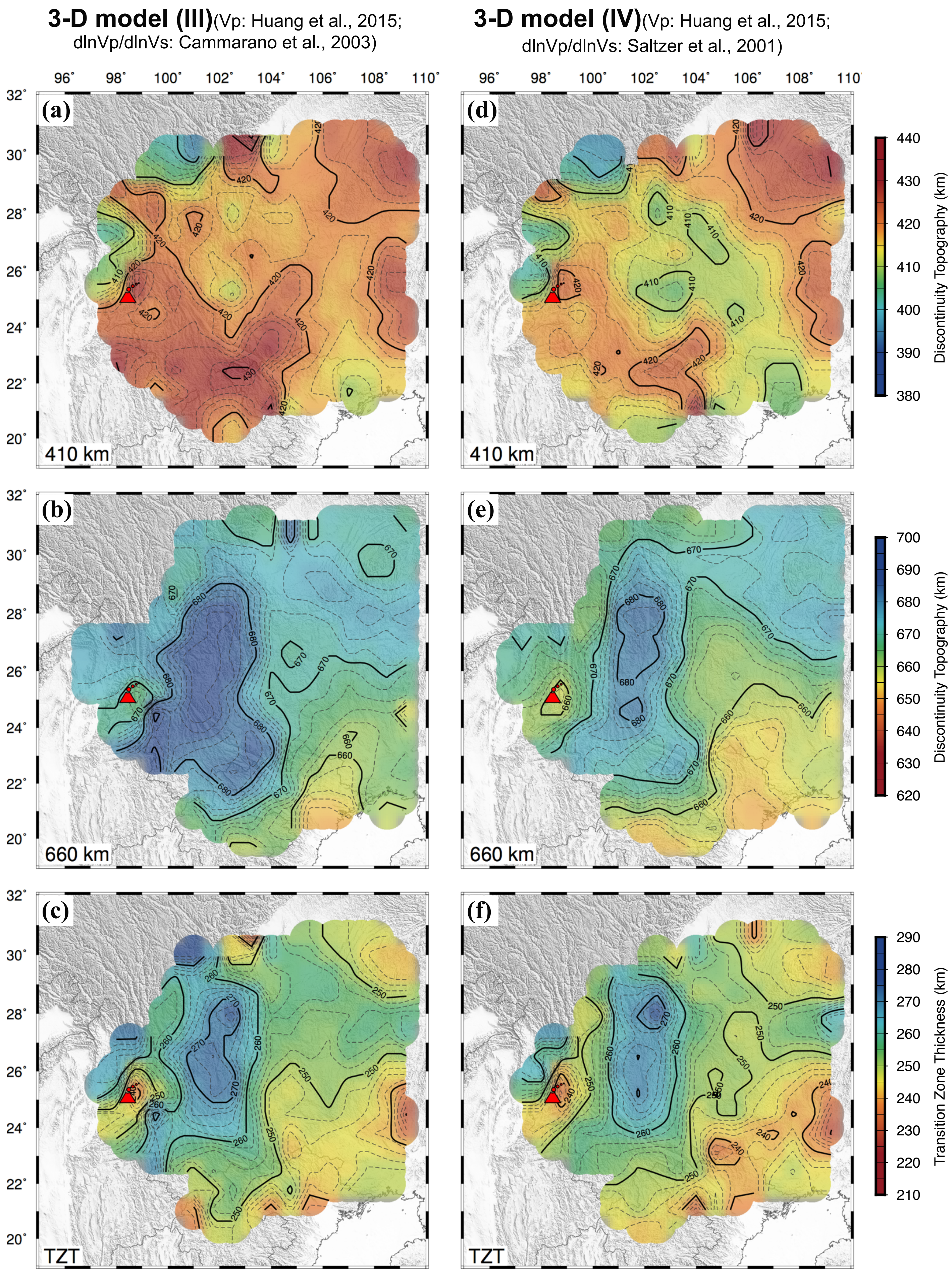

3-D model (III)(Vp: Huang et al., 2015; dlnVp/dlnVs: Cammarano et al., 2003)
3-D model (IV)(Vp: Huang et al., 2015; dlnVp/dlnVs: Saltzer et al., 2001)
(a)
(b)
(c)
(d)
(e)
(f)
410 km
660 km
TZT
Discontinuity Topography (km)
Transition Zone Thickness (km)

Figure 6

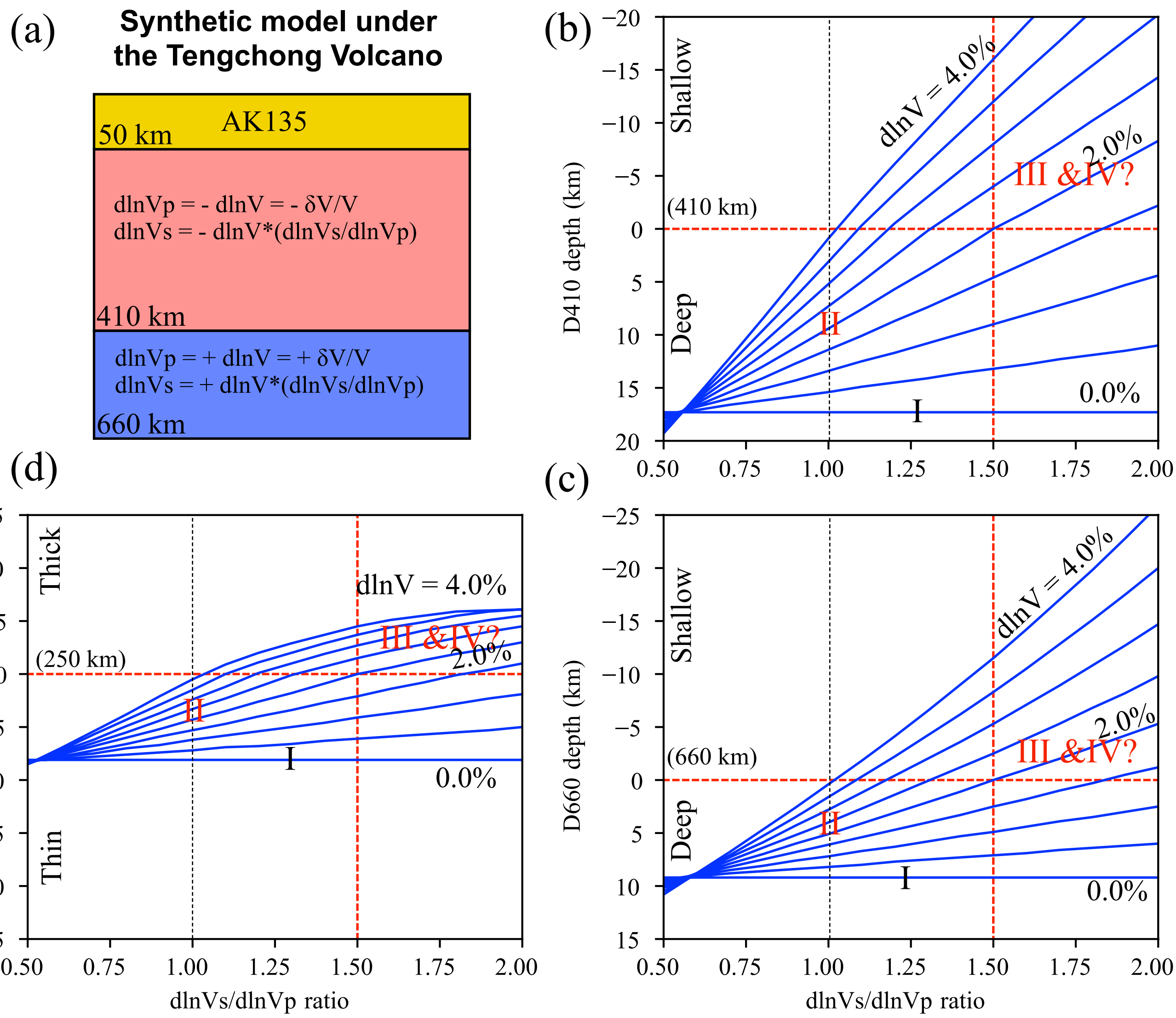

(a)
Synthetic model under the Tengchong Volcano
AK135
50 km
dlnVp = - dlnV = - δV/V
dlnVs = - dlnV*(dlnVs/dlnVp)
410 km
dlnVp = + dlnV = + δV/V
dlnVs = + dlnV*(dlnVs/dlnVp)
660 km
(b)
D410 depth (km)
Shallow
Deep
dlnV = 4.0%
2.0%
0.0%
III &IV?
II
I
(410 km)
(c)
D660 depth (km)
(660 km)
dlnVs/dlnVp ratio
(d)
MTZ thickness (km)
Thick
Thin
(250 km)
dlnV = 4.0%

Figure 7

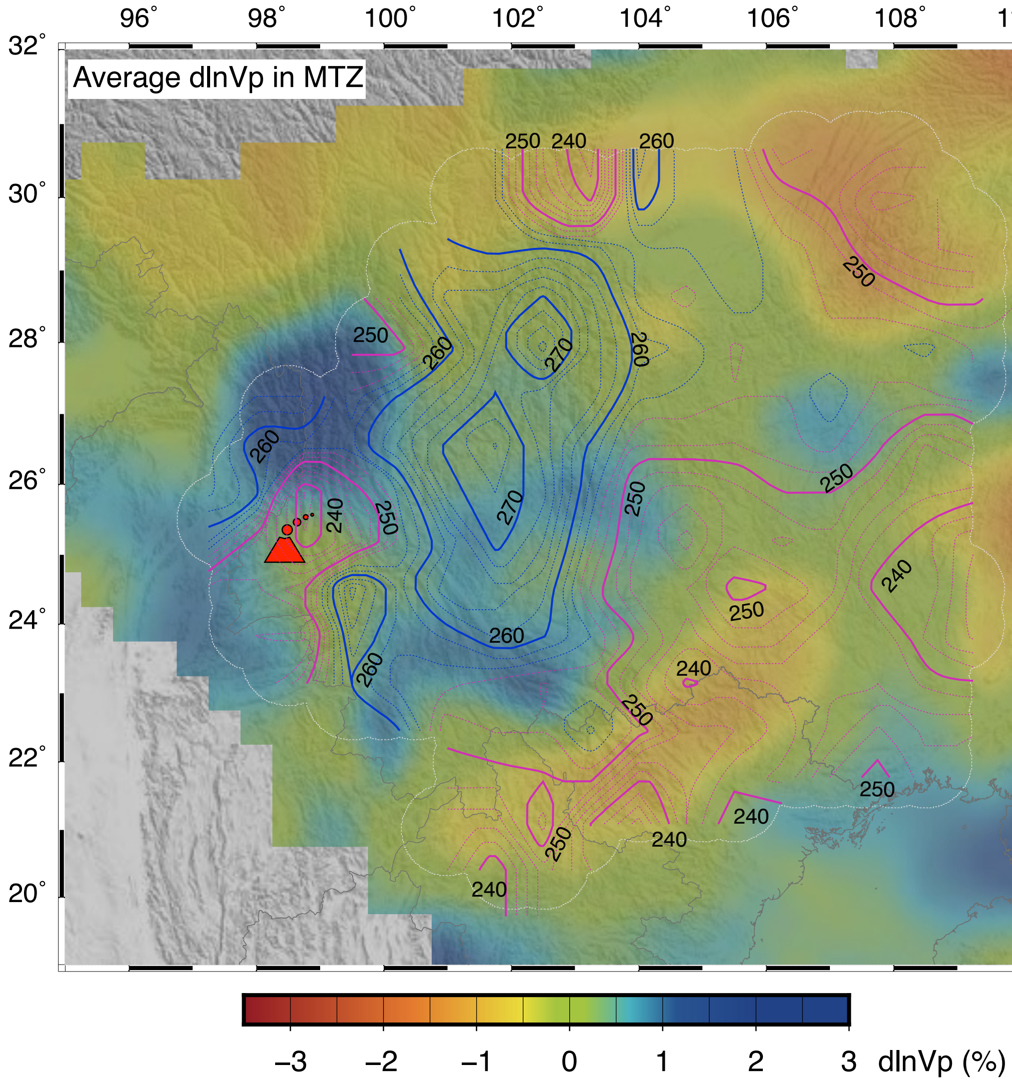

Average dlnVp in MTZ
96° 98° 100° 102° 104° 106° 108° 110°
32° 30° 28° 26° 24° 22° 20°
250
240
260
270
−3 −2 −1 0 1 2 3 dlnVp (%)

Figure 8

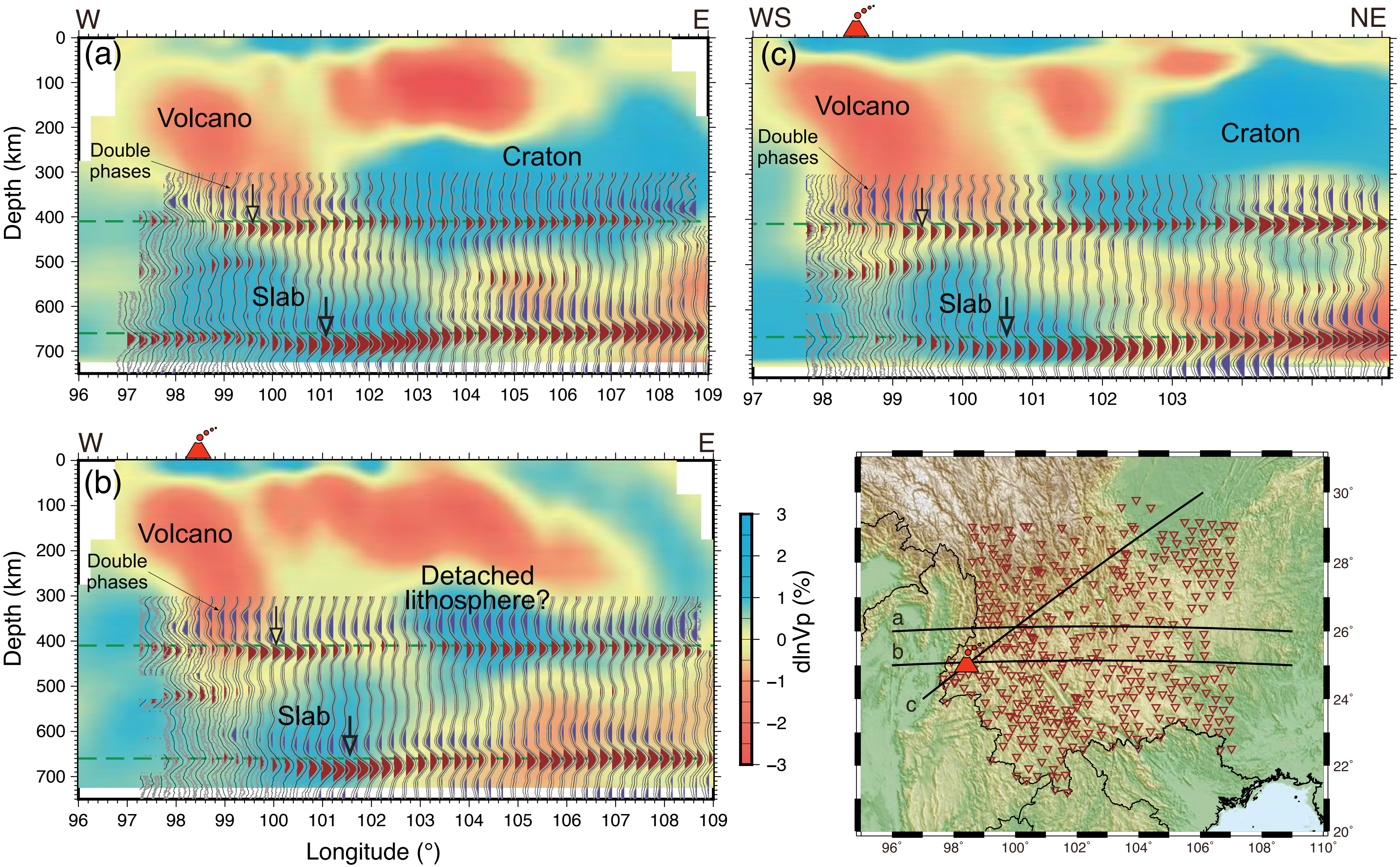
W
E
(a)
Volcano
Craton
Double phases
Slab
Depth (km)
0
100
200
300
400
500
600
700
96
97
98
99
100
101
102
103
104
105
106
107
108
109
WS
NE
(c)
Volcano
Craton
Double phases
Slab
97
98
99
100
101
102
103
(b)
Volcano
Double phases
Detached lithosphere?
Slab
Longitude (°)
dlnVp (%)
3
2
1
0
−1
−2
−3
a
b
c
30°
28°
26°
24°
22°
20°
96°
98°
100°
102°
104°
106°
108°
110°

Figure 9

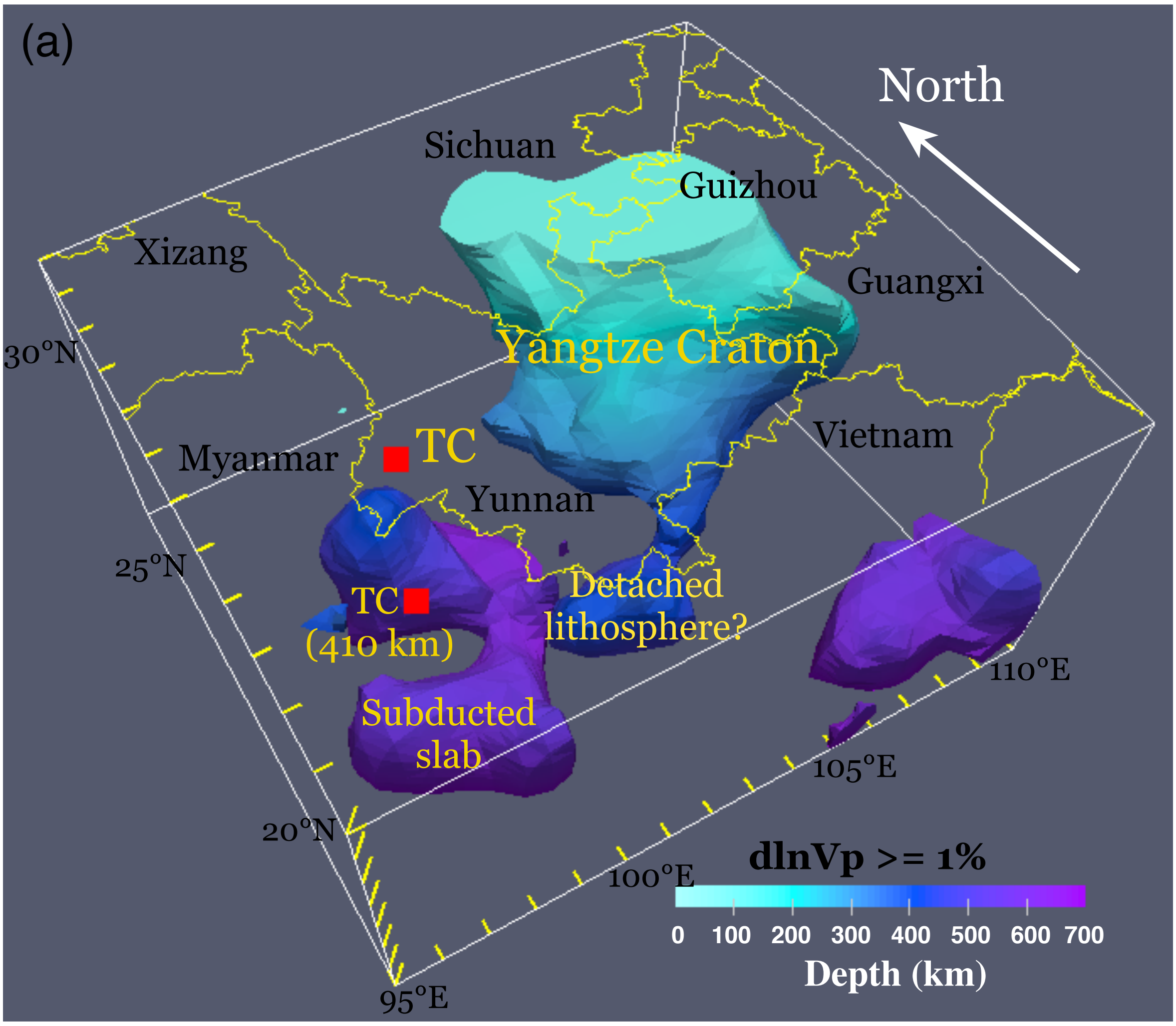
(a)
North
Sichuan
Guizhou
Xizang
Guangxi
30°N
Yangtze Craton
Vietnam
Myanmar
TC
Yunnan
25°N
TC
(410 km)
Detached
lithosphere?
110°E
Subducted
slab
105°E
20°N
dlnVp >= 1%
100°E
0 100 200 300 400 500 600 700
Depth (km)
95°E

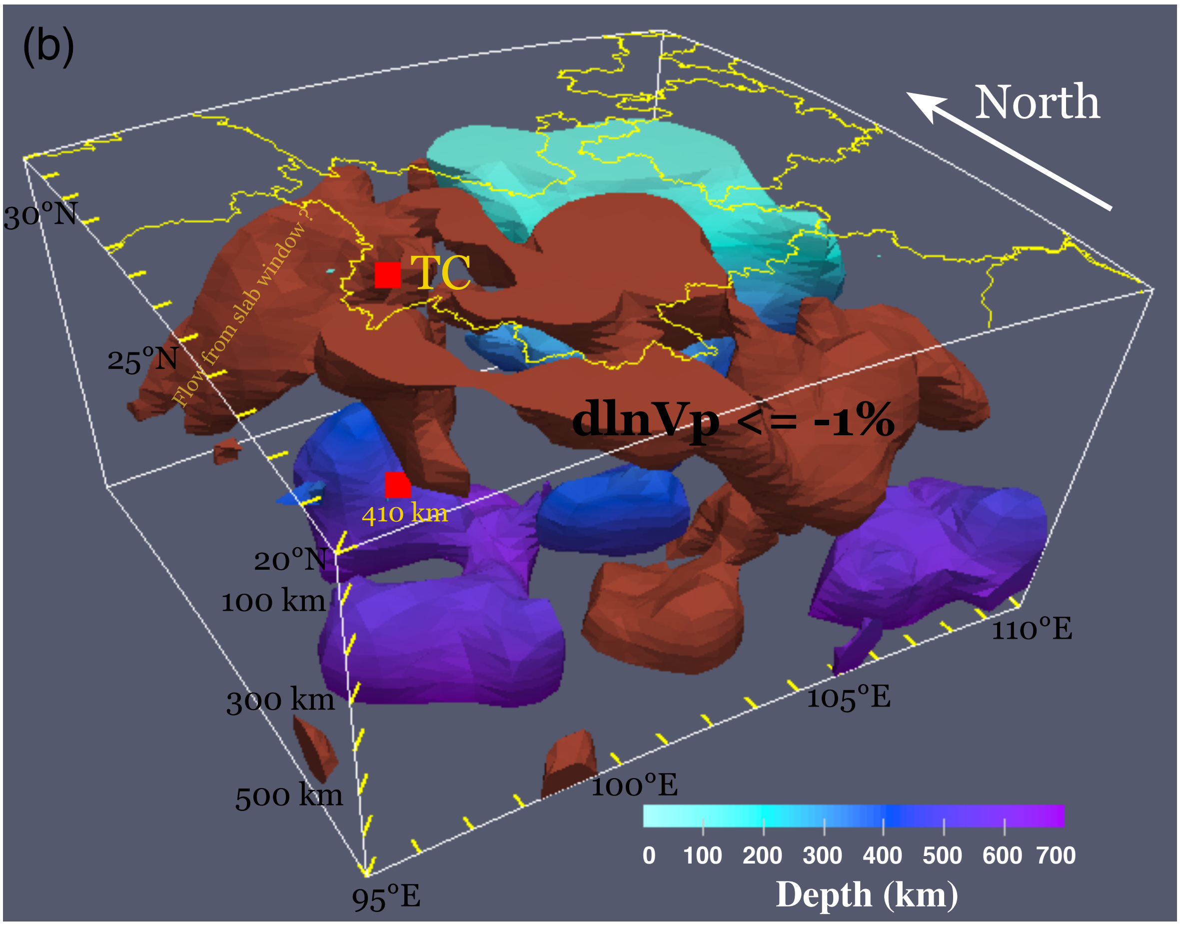
(b)
North
30°N
TC
25°N
dlnVp <= -1%
410 km
20°N
100 km
110°E
300 km
105°E
500 km
100°E
0 100 200 300 400 500 600 700
Depth (km)
95°E

Figure 10

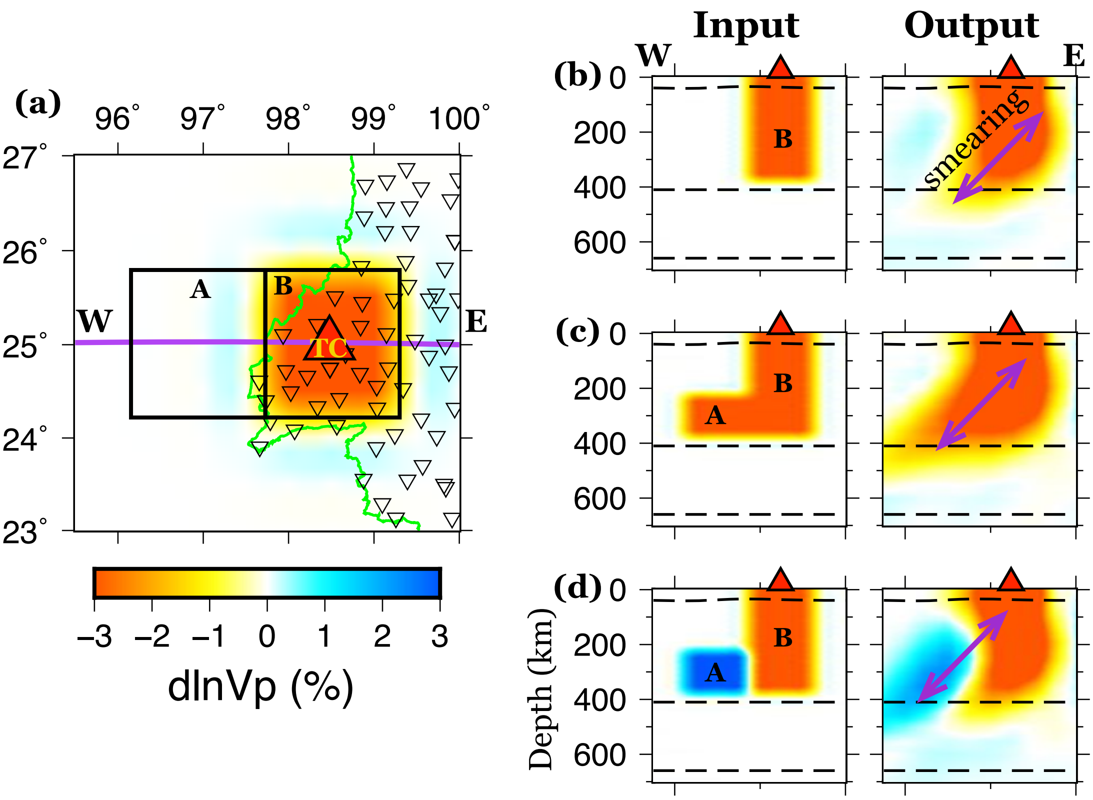
(a)
96° 97° 98° 99° 100°
27° 26° 25° 24° 23°
W
E
A
B
TC
−3 −2 −1 0 1 2 3
dlnVp (%)
Input
Output
W
E
(b)
(c)
(d)
0 200 400 600
Depth (km)
B
A
smearing